JOURNAL OF MICROENCAPSULATION
2025, VOL. 42, NO. 8, 802–819
https://doi.org/10.1080/02652048.2026.2669785

Taylor & Francis
by informa

RESEARCH ARTICLE

Check for updates

Transdermal delivery of *Astragalus tomentosus* hyaluoleosomes assisted by hollow microneedles for managing rheumatoid arthritis: *in-vitro* evaluation and biological studies

Mariam Zewail[a], Haidy Abbas[a], Nesrine El Sayed[b], Mohamed Fayez Dekinash[a,c], Reham Mustafa[a,c] and Heba Abd- El-Azim[a,d]

[a]Department of Pharmaceutics, Faculty of Pharmacy, Damanhour University, Damanhour, Egypt; [b]Department of Pharmacology and Toxicology, Faculty of Pharmacy, Cairo University, Cairo, Egypt; [c]Department of Pharmacognocy, Faculty of Pharmacy, Damanhour University, Damanhour, Egypt; [d]Postdoc Brigham and Women's Hospital, Harvard Medical School, Harvard University, Boston, MA, USA

ABSTRACT

Aim: To develop and evaluate Astragalus tomentosus (AST)-loaded hyaluoleosomes delivered via hollow microneedles as a novel approach for rheumatoid arthritis (RA) management.

Methods: AST-loaded hyaluoleosomes were prepared and characterized for particle size, polydispersity index, zeta potential, and *in vitro* drug release. The optimized formulation was intradermally administered using hollow microneedles in antigen-induced arthritis rats. Therapeutic efficacy was assessed by measuring inflammatory markers (TNF-α, IL-1, MMP-9), antioxidant markers (HO-1, NRF2, SOD), and histopathological changes.

Results: The optimized formulation showed nanosized particles (~217 nm), low PDI, and stable zeta potential, with sustained drug release over 96 h. *In vivo*, it significantly reduced joint swelling, suppressed inflammatory mediators, restored antioxidant markers, and improved histopathological features with reduced synovial inflammation and cartilage damage.

Conclusion: AST-loaded hyaluoleosomes delivered via microneedles offer a minimally invasive and effective RA treatment, demonstrating synergistic therapeutic effects.

ARTICLE HISTORY
Received 8 May 2025
Accepted 4 March 2026

KEYWORDS
Active targeting; autoimmune diseases; solid microneedles; nanovesicle; hyaluronic acid; phytosomes; *Astragalus tomentosus*

1. Introduction

Rheumatoid arthritis (RA) is an inflammatory autoimmune disease whose aetiology begins with synovitis, which refers to the inflammation and swelling of the joint capsule. This causes pannus development, which worsens joint deterioration and leads to fibrous ankylosis, then bony ankylosis (Zewail 2021). Increased knowledge of the aetiology of RA has significantly aided in the creation of efficient RA treatment regimens. Current RA therapeutic therapies, such as nonsteroidal anti-inflammatory medications (NSAIDs), disease-modifying anti-rheumatic medicines (DMARDs), glucocorticoids (GCs), and biological agents, primarily aim to alleviate RA symptoms by immunosuppression or inhibition of specific inflammatory mediators. Biological treatments such as cytokine antagonists, B cell depleting drugs, T cell co-stimulation modulators, and kinase inhibitors perform significantly better in regulating RA activity because of their specificity and selectivity (Wang *et al.* 2021). However, a large proportion of individuals exhibit decreased response after multiple administrations (Smolen and Aletaha 2015).

Nonetheless, a portion of patients do not respond well to current medications, systemic toxicity from long-term administration or distribution in non-targeted locations, and bioavailability difficulties hinder full RA remission (Wang *et al.* 2021).

Traditional medicines have long served as a first-line medication for numerous individuals worldwide. Medicinal extracts are an excellent source of therapeutic leads for the pharmaceutical sector. The use of medicinal plant treatments to treat chronic illnesses, such as RA, RA is therefore prevalent and increasing (Recio *et al.* 2012). Plants belonging to the genus *Astragalus* have been used as complementary medicine for hundreds of years. For example, *A. membranaceus* and *A. mongholicus* known as Radix Astragali are

CONTACT Mariam Zewail mariamzewail@gmail.com Department of Pharmaceutics, Faculty of Pharmacy, Damanhour University, El-Bahira, Egypt Post Office, P.O. Box 22511, Damanhour, Egypt
© 2026 Informa UK Limited, trading as Taylor & Francis Group

well-known Chinese traditional herbal medicines that are used to treat immunological disorders, enhance the circulatory system, and as hepatoprotectives and heart tonics. *Astragalus*'s (AST) phytochemical content uniformly contains major secondary metabolites, including saponins, flavonoids (glycosidic and free forms), and polysaccharides (Dekinash *et al.* 2022). Jiang *et al.* investigated the effect of AST polysaccharides on the progression and pathogenesis of RA in rats with adjuvant-induced arthritis models and their results revealed that AST polysaccharides decreased cell accumulation, oedema, joint arthritic index, and serum TNF-α and IL1-β levels in a dose-dependent manner. Also, synovial cell apoptosis increased, accompanied by elevated staining for pro-apoptotic Bax protein and reduced staining for anti-apoptotic Bcl-2 (Jiang *et al.* 2010). This is along with the findings of Maresca *et al.* that suggested that AST hydroalcoholic extract is a good candidate for RA management (Maresca *et al.* 2017).

Flavonoids are active components found in AST that have a variety of therapeutic benefits, including anti-inflammatory, immunological modulation, anti-tumour, and cardiovascular protection. However, these flavonoids have disadvantages, such as limited solubility, low permeability, limited gastrointestinal absorption, and low bioavailability (Yang *et al.* 2023).

Nanoscale medication delivery methods provide a viable solution to present therapy limitations. Nanocarriers have been proven to improve drug solubility, lengthen drug circulation time, minimise drug clearance, and deliver medications to disease locations in a regulated manner (Wang *et al.* 2020). Recently, innovative multifunctional nanocarriers with sophisticated targeted delivery or transformable features have been developed to accomplish intelligent drug delivery and improve therapeutic effectiveness (Wang *et al.* 2021).

A characteristic feature of RA is impaired angiogenesis, leading to heightened capillary permeability and the development of openings within capillary walls measuring up to 700 nm in diameter. Systemically utilised nanoparticles can passively target inflamed joints through a mechanism similar to the enhanced permeation and retention effect (EPR) observed at tumour sites. This process, referred to as '(ELVIS),' that is the abbreviation for extravasation through leaky vasculature and subsequent sequestration mediated by inflammatory cells, resulting from increased pannus vascular permeability and inflammatory cell activation (Zewail 2021, 2024, Abd-El-Azim *et al.* 2024).

Nanocarriers in RA management have been explored in various routes of administration (Abbas *et al.* 2021, Anita *et al.* 2021, Zewail *et al.* 2021a, 2021b, 2022a, Abbas *et al.* 2022, Negi *et al.* 2024). Among the most often employed tactics in transdermal drug delivery are using liposomes and liposome-like structures, like transferosomes, ethosomes, and oleosomes, as nanovesicular carriers. For example, oleosomes have been observed to boost the skin permeability of sildenafil citrate, making it a viable topical therapy for palmar-plantar erythrodysesthesia (Abdelalim *et al.* 2020). Oleic acid has well-known antioxidant and anti-inflammatory as well as penetration-enhancing properties (Santa-María *et al.* 2023). Also, among liposome-derived systems are hyalurosomes, which are a modified type of nanovesicles that combine the intrinsic properties of phospholipid nanovesicles augmented with hyaluronic acid (HA) penetration-enhancing and gelling properties. Hyalurosomes provide a synergistic effect in joints thanks to the key role of HA in joint repair and its capacity to seek out CD44receptors, which are overrepresented on macrophages in inflamed rheumatic joints. Moreover, HA is considered a crucial part of the vesicle structure that allows hyalurosomes to combine the advantages of elastic liposomes as well as the stability of gel-core vesicles (Elhalmoushy *et al.* 2022).

Combining the aforementioned liposome-derived systems to form hyaluoleosomes will result in an effective nanosystem that combines the merits of nanoencapsulation in improving RA treatment outcomes, in addition to the joint healing effects of HA and oleic acid.

In RA therapy, the joint capsule adds another barrier to transdermal medication delivery. Interestingly, microneedling devices are regarded as a simple and low-cost method for increasing cutaneous medication penetration (Abd-El-Azim *et al.* 2023). Combining nanoencapsulation with microneedles (MNs) can ensure effective drug delivery to the joint via the transdermal route. MNs are a novel skin delivery technology made up of micron-sized sharp projections arrayed in an array. They are meant to go through the stratum corneum without reaching the nerve ends, resulting in painless medication delivery (Zewail *et al.* 2024, 2025a).

Upon insertion, hollow MNs (Ho-MNs) can generate microchannels in epidermal layers, allowing vertical drug transport and promoting local drug accumulation, hence improving medication pharmacological activity. Ho-MNs offer various benefits, including the capacity to provide an exact modifiable amount of medicine and a regulated drug delivery rate (Wang *et al.* 2022, Zewail *et al.* 2024).

The main goal of the current study is the development of a novel nanosystem that can be used for

non-invasive RA management with minimum side effects using herbal medications. This was attained by encapsulating the herbal active ingredient (AST) in hyaluoleosomes that can combine the synergistic effects of HA in alleviating RA symptoms besides incorporating oleic acid that would further enhance the transdermal delivery of the hyaluoleosomes and impart extra anti-inflammatory effects. Then, AST hyaluoleosomes are intradermally injected using hollow microneedles in rats with antigen-induced arthritis model (AIA) and their pharmacological effects are assessed by measuring joint diameter, inflammatory mediator levels, and histopathological examination of dissected joints. AST-loaded phospholipid-based nanocarriers have not been prepared or explored before for RA management.

To our knowledge, this is the first study reporting the preparation of hyaluoleosomes. Also, it is the first report of AST extract loaded phospholipid vesicles that could provide a synergistic effect by combining oleic acid and HA for RA management and their intradermal administration through Ho-MNs.

2. Materials

Lipoid S 100 was a kind gift from Lipoid (Ludwigshafen, Germany). Oleic acid was purchased from Nice Chemicals (Kerala, India). High molecular weight hyaluronic acid (2MDa) was obtained from THDCHEM (Qingdao, China). AdminPen™ metallic hollow microneedles were purchased from NanoBioSciences LLC, USA. ELISA kits for haem oxygenase and nuclear respiratory factor 2 were bought from Enzo Life Sciences, New York, NY, USA and Cusabio Technology LLC, Houston, TX, USA, respectively. Tumour necrosis factor-alpha, superoxide dismutase, interleukin 1, and matrix metalloproteinases 9 were obtained from My BioSource, San Diego, CA, USA. All other chemicals are of an analytical grade.

3. Methodology

3.1. Astragalus source

Astragalus tomentosus (AST) aerial parts were collected during the fruiting stage from Rashid, about 40 km east of Alexandria, Egypt, in May 2023. Plant materials were authenticated graciously by Professor Sherif Shaarawy, Professor of Botany, Ain Shams University Faculty of Science. A voucher specimen (a.t0.1) was deposited at the herbarium of the Pharmacognosy Department, Faculty of Pharmacy, Damanhour University. The aerial parts (500 g) were air dried, pulverised, and extracted by maceration in absolute ethanol. The ethanolic extract was evaporated to dryness using a rotary evaporator at 50 °C as previously published (Dekinash *et al.* 2022).

3.2. UPLC-QqQ-MS/MS chemical profiling of AST

Analysis was conducted using UHPLC-QqQ-MS/MS (ultra-high performance liquid chromatography incorporated with triple quadrupole mass spectrometry) employing electrospray ionisation (ESI) mass spectrometry in both positive and negative modes (ESI-MS±) on a triple quadrupole instrument XEVO TQD (Waters Corporation, Milford, MA, USA). The UPLC system comprised a Waters Acquity QSM pump, an LC-2040 autosampler (Waters Corporation), a degasser, and a Waters Acquity MS detector. Chromatographic separation was performed utilising a Waters Acquity UPLC BEH C18 column (50 mm × 2.1 mm inner diameter × 1.7 µm particle size) at a temperature of 30 °C, with a sample injection volume of 5 µL and a flow rate of 0.2 mL/min. The analytical technique employed a binary mobile phase consisting of water with 0.1% v/v formic acid (phase I) and acetonitrile with 0.1% v/v formic acid (phase II). The configuration was set for gradient elution over a duration of 35 min and performed in the following sequence: 0.0–3.0 min, 10% Phase II; 3.0–6.0 min, 30% Phase II; 6.0–10.0 min, 50% Phase II; 10.0–20.0 min, 70% Phase II; 20.0–25.0 min, 80% Phase II; 26.0 min, 90% Phase II; 26.0–30.0 min, 95% Phase II; 30.0–35.0 min, 100% Phase II.

This method used UHPLC-QqQ-MS/MS in positive and negative modes to collect data from 100–1200 *m/z*. Standard working settings included 3 kV capillary voltage, 30V cone voltage, 150 °C ion source temperature, 35 psi nebuliser pressure, and 350 and 440 °C drying and sheath gas (nitrogen gas) temperatures. Sheath gas flowed 50 L/h, while drying gas flowed nine hundred L/h. Analytical runtime was 35 min. Molecular fragmentation was performed in the 2nd quadrupole Q2 utilising nitrogen to increase collision-induced dissociation energy (CID) from 30 up to 70 eV for the automatic MS/MS fragmentation of molecular ions filtered by the first quadrupole (Q1). The daughter ions were filtrated by Q3 to match the source ions' molecular structures.

To ensure data quality, the precision and repeatability were assessed using quality control samples and a standard mixture solution. During a five-day period, the standard mixture solution was continuously injected, totalling 10 injections (5 in each of the negative and positive ion modes). The data were analysed by Mzmine® 3.0.11-beta software to pre-process the raw data obtained from the UPLC-MS (peak

deconvolution, alignment, and annotation). The tandem mass spectra, including the precursor ions and the diagnostic mass fragmentation data, alongside an in-house comprehensive database encompassing all compounds documented in various *Astragalus* species globally, were employed for compound annotation. This utilised resources such as the CHEMnetBASE Dictionary of Natural Products, PubChem, and Massbank. A comprehensive presentation of the structural details of numerous compounds was provided, accompanied by a high level of annotation certainty.

3.3. Preparation of AST-loaded hyaluoleosomes

Hyaluoleosomes were prepared by the thin film hydration technique as follows: first, 160 mg of lipoid S 100 along with 30 or 50 mg of AST were dissolved in 2 mL of ethanol on the magnetic stirrer. Then, 40 mg of oleic acid was added to the mixture and stirred for an extra 10 min. Second, ethanol was evaporated at 40 °C on the magnetic stirrer. Then, the thin film was rehydrated with a 0.5% w/v HA solution containing 0.2% v/v Tween 80. Finally, the former dispersion was subjected to ultrasonication at 60% amplitude for 2 min. To prepare blank hyaluoleosomes, the same procedure was followed with the exception that we did not add AST to the lipid phase.

3.4. Characterisation of ASR-loaded hyaluoleosomes

3.4.1. Particle size, polydispersity index (PDI), and zeta potential

Measurements of particle size, PDI, and zeta potential were conducted using the Nanotrac/Wave II/Q/Zeta from Microtrac MRB (VERDER SCIENTIFIC GmbH & Co. KG, Haan, Germany) following sample dilution, with all measurements performed at room temperature.

3.4.2. Morphological examination

The morphological examination of the selected formulation was performed using a transmission electron microscope (TEM) (JEM-1400; JEOL, Japan) following staining with 1% uranyl acetate.

3.4.3. Entrapment efficiency (% EE) and drug loading %

AST-loaded hyaluoleosomes formulations were separated from the supernatant containing excess unentrapped AST through centrifugal ultrafiltration utilising a Centrisart®-I tube (MWCO 300 kDa, Sartorius AG, Goettingen, Germany). The concentration of unentrapped AST in the supernatant was quantified using UV spectroscopy at 265 nm (Chaturvedula and Prakash 2013) using the equation previously reported by Zewail *et al.* (2025b). The drug loading % was also determined by quantifying the amount of AST in a given weight of freeze dried hyaluoleosomes (Zewail *et al.* 2019).

3.4.4. In vitro drug release and release kinetics

The release of AST from specific formulations was assessed utilising the dialysis method. The volume of AST hyaluoleosomes corresponding to 0.5 mg AST was placed in a dialysis bag (Spectra/Por® membrane MWCO 100 000 Spectrum). Bags were sealed at both ends and immersed in PBS pH 7.4 to maintain sink conditions, followed by incubation in a shaking water bath at 37 ± 0.5 °C at 100 rpm (Lu *et al.* 2019). Aliquots of 1 mL were extracted from the release medium at specified time intervals and substituted with fresh phosphate buffer. AST concentration was measured using spectrophotometry at a wavelength of 265 nm (Chaturvedula and Prakash 2013). The experiment was conducted in triplicate. Release results were analysed using various kinetic models, including zero-order, first-order, Higuchi, and Korsmeyer Peppas models with the aid of DDsolver software.

3.4.5. Evaluation of stability

Optimised AST hyaluoleosomes formulation was stored in airtight amber glass bottles at 4 °C, and stability was monitored for three months. Formulations were initially examined visually for signs of physical instability, including precipitation, aggregation, or separation. Subsequently, samples were analysed for particle size, polydispersity index (PDI), zeta potential, and encapsulation efficiency (EE%).

3.5. Intradermal injection utilising the AdminPen™ hollow microneedle array (Ho-MNs)

Full-thickness intact human skin was donated by a male volunteer following abdominal plastic surgery. Subcutaneous fats were initially detached using suture scissors. The skin surface was cleansed with normal saline, dried, wrapped in aluminium foil, and stored at −20 °C. Reports indicate that, under these conditions, human skin may be preserved for up to six months (Dragicevic-Curic *et al.* 2010).

The AdminPen™, which consists of 43 stainless steel metallic Ho-MNs of 1200 m length located within 1 cm^2 of a circular MN array, was used to inject HYP solution and HYP-NLCs into the upper surface of washed full-thickness human skin. The AdminPen™ Ho-MNs were inserted into the skin using the thumb and index finger technique.

3.5.1. Assessment of hollow microneedle-assisted delivery of AST-loaded hyaluoleosomes

3.5.1.1. Ex vivo puncture-ability of microneedles. The *ex vivo* puncture-ability of AdminPen™ Ho-MNs was evaluated as previously reported with some modifications (Abd-El-Azim *et al.* 2022, Zewail *et al.* 2025b). The Ho-MNs were inserted into the skin according to the protocol stated in Section 3.3, kept for 30 s then removed. Following that, photographs of the skin were taken with a Samsung Galaxy S23 Ultra, dual pixel, PDAF camera. The percentage of percutaneous penetration was measured by counting the number of visible holes created by Ho-MNs and using the previously reported equation (Abd-El-Azim *et al.* 2024, Zewail *et al.* 2025b).

3.6. In vivo

3.6.1. RA induction and experimental design

Adult male Sprague Dawley rats (180 ± 20 g) were housed in a climate-controlled environment (25 ± 0.5 °C) with unrestricted access to a standard pellet diet and water, following a 12-h light/dark cycle. All animal experiments follow the ARRIVE guidelines and adhere to the U.K. Animals (Scientific Procedures) Act, 1986, and the National Research Council's Guide for the Care and Use of Laboratory Animals. The Faculty of Pharmacy at Cairo University approved this experimental protocol with ethical approval number PT (3462). Twenty-five male rats were allocated into five groups ($n = 5$). RA induction was conducted following the methodology established by our research group in prior publications (Abbas *et al.* 2021, 2022, Zewail *et al.* 2022a, 2025c, Abd-El-Azim *et al.* 2023). RA was induced through a single injection of 0.2 mL of complete Freund's adjuvant (CFA) into the right knee joints of rats, with the left knee joints acting as controls. Different experimental groups are illustrated in Table 1. Groups 3, 4, and 5 were treated by intradermal injection using AdminPen™ Ho-MNs on days 4 and 9 of the experiment with an AST dose of 25 mg/kg (Liu *et al.* 2017).

After 14 days, rats were anaesthetised and euthanized via cervical dislocation under thiopental anaesthesia (50 mg/kg) (Boskabady *et al.* 2011). Subsequently, joints were dissected and preserved in a 10% formalin solution. Blood samples were collected and centrifuged at 5000 rpm at room temperature for 15 min. The serum was subsequently frozen at −80 °C for later analysis.

Table 1. *In vivo* experimental groups.

Group	RA induction/treatment
Group 1	No RA induction/No treatment (Negative control).
Group 2	RA induction/Saline (Positive control).
Group 3	RA induction/AST suspension
Group 4	RA induction/AST hyaluoleosomes (F3)
Group 5	RA induction/Blank hyaluoleosomes (F1)

3.6.2. Measurements of joint diameter

The impact of different therapies on rat knee joint edoema was assessed by measuring the anteroposterior diameters of the rat knees with a digital micrometer at designated time intervals (days 0, 4, 7, and 14).

3.6.3. Enzyme-linked immunosorbent assay (ELISA)

The serum levels of haem oxygenase (HO-1) (Enzo Life Sciences, New York, NY, USA), nuclear respiratory factor 2 (NRF2) (Cusabio Technology LLC, Houston, TX, USA), tumour necrosis factor-alpha (TNFα), superoxide dismutase (SOD), interleukin 1 (IL1), and matrix metalloproteinases 9 (MMP 9) (My BioSource, San Diego, CA, USA) were assessed using an ELISA kit according to the manufacturer's instructions.

3.6.4. Histopathological study

Specimens were fixed in 10% neutral buffered formalin, decalcified in 10% formic acid, trimmed, washed in water, dehydrated in ascending grades of ethyl alcohol, cleared in xylene, and embedded in paraffin. Thin sections (4–6 µm) were processed and stained using haematoxylin and eosin stain and safranin O stain (Bancroft and Gamble 2008).

3.7. Statistical analysis

Results are represented as the mean ± *SD*. Statistical analysis were carried out using Prism 10.4.1 software. Analysis of hyalurosomes particle size and zeta potential was conducted using a Student *t*-test ($p < 0.05$), while the results of ELISA were analysed using one-way ANOVA followed by Tukey test for multiple comparison ($p < 0.0001$). Moreover, two-way ANOVA followed by the Tukey test ($p < 0.0001$) was used to analyse joint diameter results.

4. Results and discussion

4.1. Phytochemical profiling of the AST extract

4.1.1. Saponin glycosides

It is well-known that plants in the genus AST are rich in saponin glycosides. There have been reports of both cycloartane and oleanane saponins, with the latter being more prevalent (Ionkova *et al.* 2014). Using ESI-MS/MS, 7 compounds were identified as saponin glycosides from the AST extract under study, demonstrating a significant abundance of these compounds. Prominent $[M-1]^-$ peaks in compounds **15**, **18**, **20**, **21**,

22, **23**, and **24** were inferred to be saponin glycosides (Table 2).

Astraolesaponin E2 has been designated for compound **15**. The quasi-molecular ion peak $[M-1]^-$ was observed at 809 *m/z*. Dissociation of the terminal xylose moiety and the glucuronic acid component was evidenced by the daughter peaks observed at 677 *m/z* $[M-1\text{-Xylose}]^-$ and 501 *m/z* [M-1-Xylose-Glucuronic acid]$^-$, respectively (Zhang *et al.* 2016).

Compound **22** exhibited a major signal at 941 *m/z*, indicative of the quasi-molecular ion $[M-1]^-$, which was succeeded by sequential losses of the rhamnose component, resulting in a daughter peak at 795 *m/z* $[M-1\text{-Rhamnose}]^-$. This was followed by the loss of the galactose moiety, yielding a peak at 633 *m/z* $[M-1\text{-Rhamnose-Galactose}]^-$, and subsequently, Dissociation of the glucuronic acid produced the genin peak observed at 439 *m/z*. The signal at 439 *m/z* indicated the presence of a genin characterised by a triterpene nucleus comprising thirty carbon atoms (Shawky *et al.* 2022). Thus, compound **22** has been recognised as soyasaponin I.

Compound **24** was assigned to Sieberoside I. A noticeable base peak at 651 *m/z* was generated that corresponded to $[M-1]^-$. Compound **24**'s designation as a sieberoside was validated by a daughter signal at 489 *m/z*, which corresponds to the breakdown of the glycosidic bond and the loss of the sugar moiety $[M-1\text{-Glu}]^-$I (Verotta *et al.* 1998).

4.1.2. Fatty acids

Fatty acids were identified as basic cellular constituents that functioned as structural and energy-storing components. They are now regarded as essential signalling molecules involved in a wide range of metabolic processes (Verotta *et al.* 1998). The UPLC-QqQ-MS/MS chemical profiling of *Astragalus* extract identified significant mass values of key ions along with a series of 7 fatty acids. Compounds **36**, **34**, **31**, and **30** were identified as the saturated fatty acids: stearic acid, palmitic acid, myristic acid, and margaric acid, respectively. Compounds **35**, **33**, and **32** were identified as the unsaturated fatty acids: oleic acid, palmitoleic acid, and linoleic acid, respectively.

The comprehensive MS profile of compound **32** exhibited a significant peak at 279 *m/z*, indicative of the quasi-molecular ion $[M-1]^-$. A signal at 261 *m/z* suggests the elimination of a water molecule $[M-1\text{-}H_2O]^-$ (Della Corte *et al.* 2015), while another daughter peak at 235 *m/z* corresponds to the loss of CO_2 [M-1–44] (Kerwin *et al.* 1996, Koch *et al.* 2021). As a result, compound **32** has been identified as linoleic acid.

Compound **34** has been identified as palmitic acid, exhibiting its parent peak at 255 *m/z*, which corresponds to $[M-1]^-$ (Farag *et al.* 2014). The daughter peaks observed at 237 and 211 *m/z* are indicative of loss of water $[M-1\text{-}H_2O]^-$ and palmitic acid decarboxylation $[M-1–44]^-$ (Kerwin *et al.* 1996), respectively.

In all the mass spectra of the fatty acids identified in the *Astragalus* extract under study, the deprotonated molecular ion peaks $[M-1]^-$ were the dominating ions. The negative ion mode (ESI) readily ionises the carboxylic groups in the fatty acids, resulting in the formation of the quasi-molecular ion peaks $[M-1]^-$ (Koch *et al.* 2021). One water molecule was likely lost in the observed ion series $[M-1–18]^-$, water loss and carbon chain rearrangement $[H_2O + 3H + C_2H_3]$ was likely represented by the ion series $[M-1–50]^-$, and the ion series 87 was explained by McCafferty (Murad *et al.* 2014, Selim *et al.* 2023). In keeping with prior research, the linear hydrocarbon chain fragments were notably lacking. Nonetheless, the entire mass spectra of the identified fatty acids showed daughter peaks corresponding to $[M-1–44]^-$ because of fatty acids' decarboxylation (Koch *et al.* 2021).

4.1.3. Caffeic acid derivatives

Caffeic acid derivatives are among the prevalent phenolic acid derivatives found in plants. They have a wide range of biological functions and medicinal uses (Jiang *et al.* 2005, Silva *et al.* 2014). Only Compound **16** was identified in the studied AST species as a caffeic acid derivative. Compound **16** generated the quasi-molecular ion peak $[M-1]^-$ at 353 *m/z* and a noticeable signal at 752 *m/z* that represented $[2M + HCOO]^-$. The deprotonated caffeic acid ion was represented by the signal at 179 *m/z*, while quinic acid and its dehydrated form were represented by the daughter peaks at 191 and 173 *m/z* in the entire mass spectrum. Compound **16** was thus identified as chlorogenic acid (Willems *et al.* 2016).

4.1.4. Selenium containing amino acids

The optimum selenium forms for supplementation are believed to be organic forms called seleno-amino acids. Because organic forms of selenium have been shown to be less hazardous than inorganic forms, they are considered to be beneficial dietary supplements. Selenomethionine has the highest bioavailability of all the seleno-amino acids at over 90%, which is significantly higher than selenite (Hu *et al.* 2022).

UPLC-MS/MS analysis of AST identified two seleno-amino acids using ESI in positive ion mode. The complete MS profile of compound **2** exhibited a signal

Table 2. The identified phytochemicals in the *AST* extract using UPLC-MS/MS in positive and negative ionisation modes.

No.	R_t (min)	Identified compounds	Chemical class	Molecular weight	Elemental composition	Precursor ion	MS^n ions *m/z*
1	0.72	Swainsonine N-oxide	Indolizidine alkaloid	189	$C_8H_{15}NO_4$	$[M-1]^-$ 188	96, 114, 120, 143
2	0.73	3-(Methylseleno)alanine	Seleno-amino acid	182.08	$C_4H_9NO_2Se$	$[M+1]^+$ 183	166, 148, 122
3	0.74	Selenomethionine	Seleno-amino acid	196.10	$C_5H_{11}NO_2Se$	$[M+1]^+$ 197	179, 133, 103
4	0.98	Fertaric acid	Cinnamate ester	326.25	$C_{14}H_{14}O_9$	$[M-1]^-$ 325	193, 149, 134
5	3.72	Isorhamnetin 3-glycosides 3-O-[β-D-Apiofuranosyl-(1→2)-[α-L-rhamnopyranosyl-(1→6)]-β-D-galactopyranoside]	Flavonoidal glycoside	756.66	$C_{33}H_{40}O_{20}$	$[M-1]^-$ 755	593, 447, 315
6	4.28	Ascaside	Flavonoidal glycoside	740.66	$C_{33}H_{40}O_{19}$	$[M-1]^-$ 739	575, 395, 231
7	6.45	Apiin	Flavonoidal glycoside	564.49	$C_{26}H_{28}O_{14}$	$[M-1]^-$ 563	563, 401, 269
8	6.74	Flagaloside D	Flavonoidal glycoside	580.49	$C_{26}H_{28}O_{15}$	$[M-1]^-$ 579	447, 315
9	7.03	Kaempferol 3-diglucoside	Flavonoidal glycoside	610.52	$C_{27}H_{30}O_{16}$	$[M-1]^-$ 609	285, 151, 133
10	7.05	Quercetin-3,7-di-O-β-glucoside	Flavonoidal glycoside	625.51	$C_{27}H_{29}O_{17}$	$[M-1]^-$ 624	462, 300, 299, 121, 151, 178
11	7.09	Isorhamnetin 3-O-diglycoside	Flavonoidal glycoside	624.54	$C_{28}H_{32}O_{16}$	$[M-1]^-$ 623	443, 279, 264, 151
12	7.52	Salviolinic acid	Phenolic acid	716.9	$C_{36}H_{29}O_{16}$	$[M-1]^-$ 715	671, 687, 607
13	7.58	Rhoifolin	Flavonoidal glycoside	′578.52	$C_{27}H_{30}O_{14}$	$[M-1]^-$ 577	269, 151, 116
14	7.96	Odoratin 7-glucoside	Flavonoidal glycoside	476.43	$C_{23}H_{24}O_{11}$	$[M-1]^-$ 475	313, 282
15	8.29	Astraolesaponin E2	Saponin glycoside	810.92	$C_{41}H_{62}O_{16}$	$[M-1]^-$ 809	677, 501
16	8.59	Chlorogenic acid	Caffeic acid	354.31	$C_{16}H_{18}O_9$	$[M-1]^-$ 353	191, 173, 179
17	8.89	Astragalin	Flavonoidal glycoside	448.38	$C_{21}H_{20}O_{11}$	$[M-1]^-$ 447	285, 257, 151
18	9.69	16,23-Epoxy-24,25,26,27-tetracycloartane-3,6,23-triol (3β,6α,16β,23 R)-form, 6-Ac, 3-O-[2E-butenoyl-(1→4)-β-D-xyloside]	Saponin glycosides	660.83	$C_{37}H_{56}O_{10}$	$[M-1]^-$ 659	527, 509
19	10.27	Cirsiliol	Dimethoxy flavone	330.29	$C_{17}H_{14}O_7$	$[M-1]^-$ 329	314
20	10.61	Dasyanthoside A	Saponin glycosides	712.86	$C_{37}H_{60}O_{13}$	$[M-1]^-$ 711	683, 579, 447
21	10.62	Laceioside	Saponin glycosides	969.91	$C_{38}H_{64}O_{11}$	$[M-1]^-$ 968	806, 761
22	11.40	Soyasaponin I	Saponin glycosides	942.98	$C_{48}H_{78}O_{18}$	$[M-1]^-$ 941	795, 633, 439
23	11.64	Prusianoside A	Saponin glycosides	664.82	$C_{36}H_{56}O_{11}$	$[M-1]^-$ 663	501, 483
24	12.24	Sieberoside I	Saponin glycosides	652.85	$C_{36}H_{60}O_{10}$	$[M-1]^-$ 651	651, 489
25	14.80	Rhamnetin	Flavonol	316.26	$C_{16}H_{12}O_7$	$[M-1]^-$ 315	165, 121
26	15.22	Daidzein	Isoflavone	254.24	$C_{15}H_{10}O_4$	$[M-1]^-$ 253	135, 117
27	15.56	Calycosin	Isoflavone	284.26	$C_{16}H_{12}O_5$	$[M-1]^-$ 283	269, 136, 148
28	15.89	Afromosin	Isoflavone	297.81	$C_{17}H_{14}O_5$	$[M-1]^-$ 296	281
29	17.37	11-p-Coumaroylnepeticin	Triterpenoid	588.86	$C_{39}H_{56}O_4$	$[M-1]^-$ 587	441, 427, 399, 223, 205
30	18.91	Margaric acid	Fatty acid	270.45	$C_{17}H_{34}O_2$	$[M-1]^-$ 269	251, 207
31	20.38	Myristic acid	Fatty acid	228.37	$C_{14}H_{28}O_2$	$[M-1]^-$ 227	209, 183
32	21.80	Linoleic acid	Fatty acid	280.40	$C_{18}H_{32}O_2$	$[M-1]^-$ 279	261, 235
33	22.69	Palmitoleic acid	Fatty acid	254.41	$C_{16}H_{30}O_2$	$[M-1]^-$ 253	235, 191
34	24.20	Palmitic acid	Fatty acid	256.42	$C_{16}H_{32}O_2$	$[M-1]^-$ 255	237, 211

(*Continued*)

Table 2. Continued.

No.	R_t (min)	Identified compounds	Chemical class	Molecular weight	Elemental composition	Precursor ion	MS^n ions *m/z*
35	24.68	Oleic acid	Fatty acid	282.46	$C_{18}H_{34}O_2$	$[M-1]^-$ 281	263, 219
36	27.92	Stearic acid	Fatty acid	284.48	$C_{18}H_{36}O_2$	$[M-1]^-$ 283	265, 221

at 183 *m/z*, indicative of the quasi-molecular ion parent peak. The signal at 166 *m/z* corresponds to the loss of ammonia $[M+1\text{-}NH_3]^+$, while the signals at 148 and 122 *m/z* correspond to the loss of water besides the ammonia $[M+1\text{-}NH_3\text{-}H_2O]^+$, and the loss of carbon dioxide besides the ammonia $[M+1\text{-}NH_3\text{-}CO_2]^+$, respectively. The identified pieces aligned with the mass fragmentation profile of 3-(Methylseleno)alanine, also referred to as methylselenocysteine (Zou *et al.* 2022). Compound **3** exhibited the quasi-molecular ion peak $[M+1]^+$ at 197 *m/z*. Signals at 179 and 133 *m/z* indicated the elimination of ammonia $[M+1\text{-}NH_3]^+$, and the loss of water, ammonia, and carbonyl group $[M+1\text{-}NH_3\text{-}CO\text{-}H_2O]^+$, while the signal at 103 *m/z* indicated the formation of a non-selenium-containing fragment resulting from the cleavage of selenium and its corresponding methyl group $[M+1\text{-}CH_3Se]^+$. Consequently, component 2 was identified as selenomethionine (Kurek *et al.* 2020, Zou *et al.* 2022).

4.1.5. Flavonoids

The genus AST encompasses a variety of subclasses of flavonoids, including flavonols, flavanonols, flavones, flavanones, chalcones, isoflavones, isoflavanes, aurones, and pterocarpans, all of which have been thoroughly documented (Fu *et al.* 2014). The analysed AST extracts demonstrated a significant presence of flavonoidal glycosides encompassing various aglycon subclasses, including flavones, isoflavones, and flavonols. In the current investigation, ten flavonoidal glycosides and five free aglycones were tentatively identified.

Commencing with flavonoidal glycosides, compound **8** was provisionally annotated as flagaloside D, exhibiting the quasi-molecular ion peak $[M-1]^-$ at 579 *m/z*. In the MS/MS spectrum, two successive daughter peaks were observed at *m/z* 447 and 315, signifying the elimination of the two xylose molecules $[M-1\text{-}2Xyl]^-$ (Sheng *et al.* 2021). Kaempferol-3-diglucoside, denoted as compound **9**, displayed a pronounced quasi-molecular ion signal $[M-1]^-$ at 609 *m/z*. The breakdown of the two glucose molecules accounts for the genin signal at 285 *m/z* $[M-1\text{-}2Glu]^-$, arising from the inherent instability of the residual aglycone's ring C, which is predisposed to cleavage, subsequently yielding additional fragments at 133 and 151 *m/z* (Bratkov *et al.* 2016) due to retro-Diels Alder (Elhalmoushy *et al.* 2022).

Compounds **10** and **11** produced parent peaks at 623 and 624 *m/z*, respectively, corresponding to the pertinent peak $[M-1]^-$ of the quasi-molecular ions. The compounds were identified as quercetin-3,7-di-*O*-*β*-glucoside and isorhamnetin-3-*O*-diglucoside, respectively, and subjected to fragmentation following the same pattern as compound **13**, given that they are all classified as flavonol glycosides (Bratkov *et al.* 2016, Sheng *et al.* 2021). Conversely, certain compounds were recognised as flavonoidal aglycones. Compounds **26** and **27** have been recognised as daidzein and calycosin isoflavones, respectively. The molecular ion peak for diadzein genin was characterised by the loss of two protons and the formation of a potassium ion adduct, denoted as $[M-2H+K]^-$. Additional signals were observed at 117 and 135 *m/z*, which correspond to retro Diels-Alder dissociation (Simons *et al.* 2009). Calycosin was discerned at 329 *m/z*, characterised as a formic acid adduct ion $[M+HCOOH]^-$. According to the literature, the distinctive MS/MS fragments were observed at 269 *m/z* as a result of demethylation, besides signals at 148 and 136 *m/z* as a result of C-ring cleavage (Frański *et al.* 2019).

It has been tentatively established that compound **25** is identified as the flavonol rhamnetin. The deprotonated molecular ion peak $[M-1]^-$ was observed at 315 *m/z*. A diagnostic daughter peak is observed at *m/z* 193 in the MS^2 spectrum of rhamnetin quasi-molecular ion. The ion at *m/z* 193 was observable solely at low collision energy and disappeared at elevated collision energy, unlike the other diagnostic daughter peaks (*m/z* 165 and 121), which can be attributed to retro Diels-Alder fragmentation. In contrast to other methoxylated flavonoids, rhamnetin exhibited a distinct fragmentation pattern; at low collision energy, the cleavage of the C ring leading to the formation of $[O,4B-H]^-$ daughter peak at 193 *m/z* was favoured than the loss of the methyl group (Frański *et al.* 2019).

4.1.6. Heterogenous compounds

Miscellaneous phytochemicals have been tentatively identified in the HPLC-MS/MS analysis of AST extract as 11-p-coumaroylnepeticin, fertaric acid, swainsonine N oxide, salviolinic acid, and spinocoumarin I. Compound **4**, identified as fertaric acid, showed the

deprotonated molecular ion peak at *m/z* 325 $[M-1]^-$. This compound breakdown at a higher impact energy, resulting in two daughter peaks at 193 and 149 *m/z* representing ferulic acid and tartaric acid, respectively. Also, a signal at 134 *m/z* was discovered indicating decarboxylation of ferulic acid (Buiarelli *et al.* 2010).

Compound **1** was annotated as swainsonine N-oxide. It displayed two significant signals: a quasi-molecular ion signal at 188 *m/z* associated with $[M-1]^-$ and a notable signal at 377 *m/z* representing $[2M-1]^-$. The MS^2 showed notable daughter peaks at (143, 120, 114, 96 *m/z*), which are characteristic of indolizine alkaloids (Ralphs *et al.* 2008).

Compound **12** has been designated as salviolinic acid, yielding a parent peak at 715 *m/z*, which was recognised as the quasi-molecular ion peak $[M-1]^-$. Fragment ions of salvianolic acid were discerned through the loss of water (18 Da), CO (28 Da), and CO_2 (44 Da). Consequently, the daughter peaks generated were observed at 607, 687, and 671 *m/z*, sequentially (Cheng *et al.* 2019).

4.2. Preparation and characterisation of hyaluoleosomes

Phospholipid-based vesicles possess several merits, such as biocompatibility, biodegradability, and decreased toxicity in contrast to polymeric nanoparticle drug delivery systems (Witika *et al.* 2020). Hyaluoleosomes combine the advantages of both hyalurosomes and oleosomes as they contain HA, which is essential in treating RA because it recovers the viscoelasticity of inflamed joints. Moreover, HA is considered CD44's primary ligand. It is capable of interacting with CD44v isoforms that are widely expressed, including macrophages, which are inflammatory joint cells. By binding to the cell surface CD44, HA prolongs the particles' joint residence and increases their contact with chondrocytes. The application of HA in nanocarriers might help enhance joint function and reduce pain with no adverse effects (Makled *et al.* 2024).

Furthermore, oleic acid may improve epidermal permeability by disrupting stratum corneum lipid bilayers and forming lacunae consequently promoting transdermal medication delivery (Jiang and Zhou 2003). Oleic acid is the major monounsaturated fatty acid in the human circulatory system, it has an anti-inflammatory potential and can act as an antioxidant as it can directly regulate both the synthesis and activities of antioxidant enzymes (Santa-María *et al.* 2023). Tween 80 was used in hyaluoleosomes to obtain deformable vesicles that ensure efficient transdermal distribution (Morilla and Romero 2015).

Despite that there was a previous report by El Halmoushy *et al.* for the preparation of berberine loaded core gel oleosomes by the ethanol injection technique (Elhalmoushy *et al.* 2023). The prepared vesicles were composed of phospholipids, sodium hyaluronate, and sodium oleate. This is the first report on the preparation of hyaluoleosomes using HA and oleic acid using a thin film hydration technique. Also, it is the first report of AST-loaded hyaluoleosomes.

As shown in Table 3, the mean diameter of different formulations ranged from 116 ± 0.45 to 217.5 ± 1.14 nm, suggesting their ability to penetrate the skin layers and attain great skin deposition (Elmowafy 2021). Blank hyaluoleosomes (F1) had the smallest mean diameter while AST-hyaluoleosomes loaded with 50 mg AST (F3) had the largest mean diameter. It can be noted that loading blank hyaluoleosomes (F1) with AST resulted in increasing their mean diameter (F2, F3). Also, increasing AST concentration from 30 mg (F2) to 50 mg (F3) increased their mean diameter significantly [Student's *t*-test ($p < 0.05$)] from 164.3 ± 0.89 to 217.5 ± 1.14 nm. These findings are in agreement with the results previously reported by Abdelalim *et al.*, who reported that oleosomes' mean diameter significantly increased upon increasing sildenafil concentration from 0.5 to 0.75 mg/mL (Abdelalim *et al.* 2020). Also, coincides with the results reported by Zewail *et al.*, that illustrated the particle size of hyalurosomes significantly increased upon loading with luteolin and dexamethasone (Zewail *et al.* 2025c).

The PDI value is crucial in the optimisation of the hyaluoleosomes as it assures the homogeneity of hyaluoleosomes (Zewail *et al.* 2022a, Moussa *et al.* 2023). PDI of different hyaluoleosomes ranged from 0.221 ± 0.07 (F2) to 0.277 ± 0.01 (F1); therefore, hyaluoleosomes are considered a homogenous nanodispersion.

Zeta potential is crucial for the stability of nanodispersions where stable formulations are those whose

Table 3. Composition and colloidal characteristics of hyaluoleosomes.

Formulation	AST (w/v %)	Oleic acid (w/v %)	HA (w/v %)	Mean diameter (nm)	PDI	Zeta potential (mV)	% EE	% Drug loading (w/w%)
F1	—	0.4	0.5	116 ± 0.45	0.277 ± 0.01	−14 ± 1.34	—	—
F2	0.3			164.3 ± 0.89	0.221 ± 0.07	−18.2 ± 0.98	95.23 ± 1.23	12 ± 0.56
F3	0.5			217.5 ± 1.14	0.236 ± 0.05	−22 ± 1.12	98.78 ± 2.05	20 ± 0.73

Results are represented as mean ± *SD* where, $N = 3$. Data were analysed using Student *t*-test ($p < 0.05$).

zeta potential values approach ±30 mV (Zewail *et al.* 2022b). This might be explained by the repulsive forces that inhibit particle coalescence and aggregation (Rahman *et al.* 2013, Zewail *et al.* 2019, Ahmed *et al.* 2020). All hyaluoleosomes possessed a negative surface charge that may be attributed to lipoid S 100 and oleic acid (Abdelalim *et al.* 2020). Moreover, the negative charge of HA that arises from its anionic properties and its interaction with the choline moiety in the phospholipid structure (Elsheikh *et al.* 2023). This is in agreement with the previous reports of hyalurosomes' (Manca *et al.* 2019, Elhalmoushy *et al.* 2022, Elsheikh *et al.* 2023, Makled *et al.* 2024) and olesosomes' negative surface charge (Abdelalim *et al.* 2020, Elhalmoushy *et al.* 2023). The increase in the zeta potential upon loading hyaluoleosomes with AST in F2 and F3 may be attributed to the negative surface charge of AST (Du *et al.* 2022). Also, increasing AST concentration increased the zeta potential value from −18.2 ± 0.98 mV in F2 (containing 30 mg AST) to −22 ± 1.12 mV in F3 (containing 50 mg AST).

4.3. EE % and drug loading %

Both F2 and F3 demonstrated high EE %. The higher EE % of F3 (98.78 ± 2.05) compared to F2 (95.23 ± 1.23) may be ascribed to increasing AST concentration so more drug can be incorporated into the vesicles (Abdelalim *et al.* 2020). The high EE % of hyaluoleosomes is along with previous reports of high EE % of hyalurosomes and oleosomes (Manca *et al.* 2019, Abdelalim *et al.* 2020, Elhalmoushy *et al.* 2022, 2023, Elsheikh *et al.* 2023, Makled *et al.* 2024). Drug loading % was 12 ± 0.56%w/w and 20 ± 0.73%w/w for F2 and F3, respectively, as demonstrated in Table 2.

F3 was selected for further characterisation as it had a suitable mean diameter for transdermal delivery 217.5 ± 1.14 nm. Homogenous particle size distribution and high EE % (98.78 ± 2.05).

4.4. TEM

The TEM micrograph of selected hyaluoleosomes formulation (F3) is illustrated in Figure 1(A). F3 had a spherical shape with uniform size distribution, no signs of aggregation, and a distinct core-shell structure ensuring effective coating of HA to the lipid core.

4.5. In vitro drug release

In vitro drug release was conducted for AST suspension and AST hyaluoleosomes (F3) (Figure 1(B)). AST suspension was completely released after 24 h. On the other hand, F3 demonstrated a sustained release profile that extended for 96 h with biphasic release patterns like hyalurosomes. An initial burst effect of 15% w/v was noted after 0.5 h. This complies with the previous data published on oleosomes and hyalurosomes drug release as they can provide biphasic drug release with an initial burst effect (Elhalmoushy *et al.* 2023, Makled *et al.* 2024).

After fitting release data to zero, first, Higuchi and Korsmeyer Peppas models using DDsolver. The *in vitro* release model of F3 best fit Korsmeyer Peppas model as it had the highest R^2 value (0.967) and since $n = 0.317$ release mechanism is governed by diffusion (Arora *et al.* 2011). Meanwhile, the highest R^2 value (0.983) for AST was for the first order model indicating that AST release was time-dependent (Soni and Yadav 2014).

4.6. Storage stability

No signs of instability were observed after storing F3 at 4 °C for 3 months as demonstrated in Table 4. The optimised formulations preserved their physicochemical properties, such as uniform particle size distribution and negative zeta potential. Furthermore, F3 maintained their EE% values (98.78%), indicating enhanced stability without any drug leakage. This coin sides with the previous reports of HA functionalised phospholipid vesicles (Zewail *et al.* 2025c, 2025d).

4.7. Ex-vivo insertion of Ho-MNs

In this work, we evaluated the impact of nanoencapsulation combined with Ho-MNs in overcoming poor skin penetration and delivering AST locally to manage RA. Ho-MNs can enhance bioavailability while providing the required therapeutic effect at a lower dose. Nonetheless, MNs may enable long-term drug delivery, resulting in reduced dose frequency (Gowda *et al.* 2023, Zewail *et al.* 2024).

Successful dermal piercing is critical for MNs to carry out their intended activity (Rahman *et al.* 2013). Excised human skin is regarded as the 'gold standard' for assessing *in vitro* permeation studies (Elhalmoushy *et al.* 2022). Although mice, rats, and humans have similar skin structures in the epidermis, dermis, and hypodermis, their stratum corneum thicknesses differ. In mice, it is around 5 µm, but in humans, it ranges from 10 to 20 µm (Wei *et al.* 2017). In this investigation, human skin was used to precisely imitate clinical settings. The AdminPen™ Ho-MNs (Figure 2(A)) were employed to penetrate the excised human skin. Figure

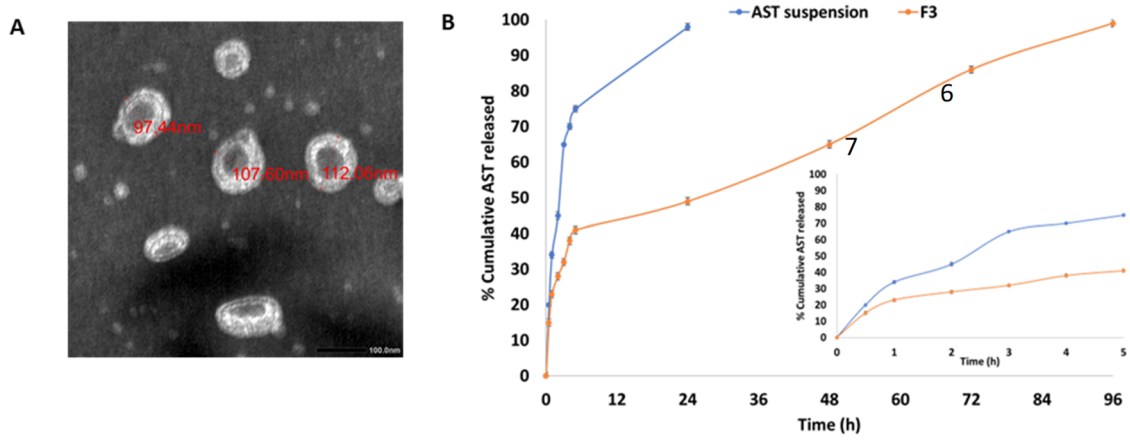


Figure 1. (A) TEM micrograph of selected hyaluoleosomes formulation (F3). (B) *In vitro* AST release from AST suspension and F3. Insert *in vitro* AST released within 5 h. Results are represented as mean ± *SD* where, $N = 3$. Data were analysed using Student *t*-test ($p < 0.05$).

Table 4. Stability of selected formulation (F3) after 1, 2, and 3 months storage at 4 °C.

Formulation	Mean diameter (nm)	PDI	Zeta potential (mV)	% EE
1 month	217 ± 0.98	0.236 ± 0.12	−22 ± 1.5	98.93 ± .05
2 months	219 ± 0.54	0.245 ± 0.15	−22.5 ± 0.98	98.89 ± 2.05
3 months	220 ± 0.87	0.246 ± 0.16	−23 ± 0.59	98.76 ± 1.05

Results are represented as mean ± *SD* where, $N = 3$. Data were analysed using Student *t*-test ($p < 0.05$).

2(C) shows that AdminPen™ Ho-MNs successfully penetrated the stratum corneum, resulting in 43 holes and 100% skin penetration (Figure 2(B)). Thus, the suggested MN-NLCs combination delivery method proved to be a viable technique for efficient transdermal administration of AST to RA affected joints.

4.8. In vivo study

RA was successfully induced in mice and rats by numerous approaches, including AIA, which has been demonstrated to be effective in producing RA-associated physiological changes (Choudhary *et al.* 2018). Prior research has demonstrated the efficacy of this induction model in inducing rheumatoid arthritis, as evidenced by histopathological analysis of the positive control dissected joints and the measurement of various inflammatory mediators (Kamel *et al.* 2016, Abbas *et al.* 2021, Zewail 2021, Zewail *et al.* 2021a, 2021b, 2022a, Abbas *et al.* 2022, Abd-El-Azim *et al.* 2023, 2024).

The transdermal route was selected to offer a non-invasive option for RA management, potentially enhancing patient compliance. Transdermal drug delivery reduces the incidence of adverse effects associated with extended systemic drug administration and avoids first-pass metabolism (Zewail *et al.* 2025c). The treatment groups administered two intradermal injections by Ho-MNs on days 4 and 9 of the experiment.

4.8.1. Joint morphology and diameter

Joint diameters for different experimental groups were assessed on days 0, 4, 7, and 14 of the study (Figure 2(D)). Statistical analysis using two-way ANOVA followed by the Tukey test ($p < 0.0001$) revealed significant differences among treatment groups in comparison to the positive control group. The group that received AST-hyaluoleosomes through MNs showed no statistically significant differences when compared to the negative control. Morphological examination of joints after the experiment (Figure 2(E)) revealed that the group treated with AST-hyaluoleosomes via MNs displayed nearly normal joint morphology and showed greater improvement compared to the group treated with AST suspension, blank hyaluoleosomes using MNs, and the positive control group.

4.8.2. ELISA

Several factors influence RA development and invasiveness. TNF-α has a prominent impact on the progression of RA. The stimulation of TNF-α is associated with the activation of various cells, including T cells, dendritic cells, and B cells, which subsequently results in T cell activation and differentiation (Abd-El-Azim *et al.* 2024). IL1 is another inflammatory mediator that is significantly elevated in the serum of rheumatoid arthritis patients when compared to those with osteoarthritis and non-inflammatory joint diseases. TNFα and IL-1 can trigger the release of MMPs, which are responsible for cartilage degradation. Additionally,

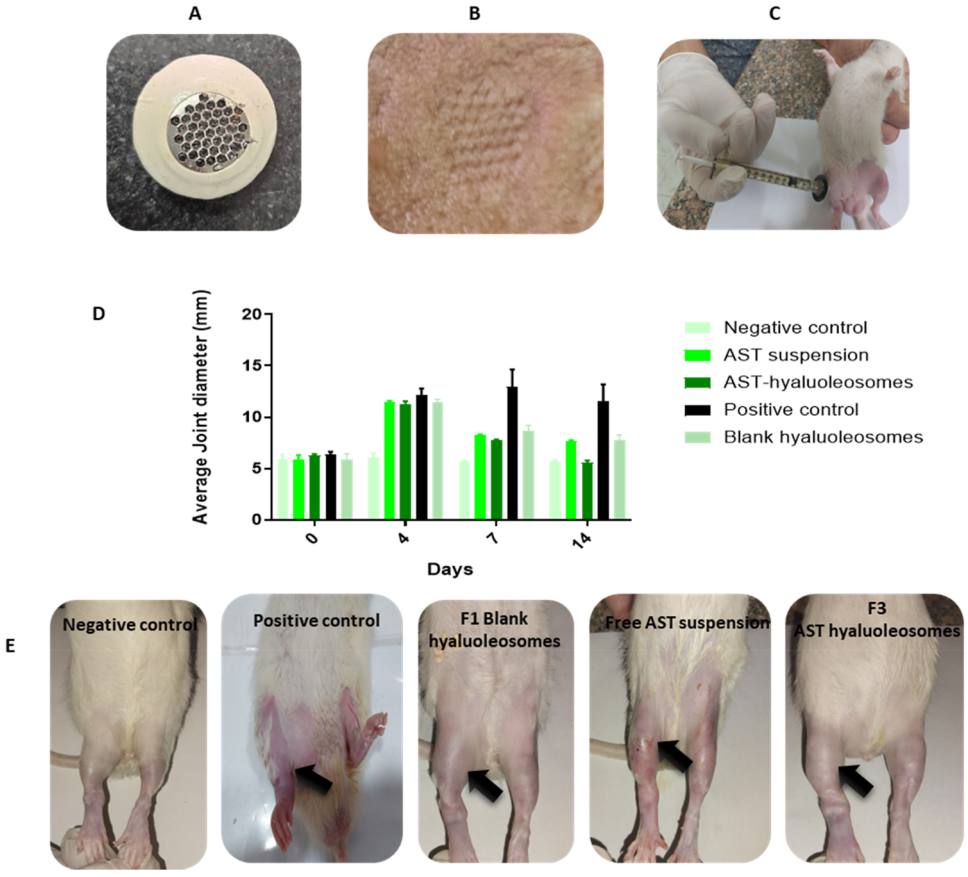


Figure 2. (A) AdminPen™ hollow MNs with 43 stainless-steel MN shafts of 1200 µm in height. (B) Image captured by a standard mobile camera (Samsung Galaxy S23 Ultra, 12 MP, dual pixel) showing excised full-thickness human skin after insertion of MNs. (C) Intradermal administration of drug formulations using AdminPen™ hollow MNs into the arthritic joint in rats with AIA. (D) Joint diameter measurements at days 0, 4, 4, and 14 in different experimental groups where, $N = 3$, Statistical analysis was conducted using two-way ANOVA followed by the Tukey test ($p < 0.0001$). (E) Morphology of different experimental group joints at the end of the experiment. Arrows represents knee joints with AIA.

they can enhance the expression of proinflammatory genes, resulting in the overproduction of various proinflammatory mediators such as nitric oxide and prostaglandin E2 (Kay and Calabrese 2004).

Also, in addition to TNFα and IL1, HO-1 plays a regulatory role in the progression of RA inflammation (Abd-El-Azim *et al.* 2024). Moreover, another contributing factor to the pathogenesis of RA is the decreased levels of NRF2. Levels of both NRF2 and SOD are downregulated in patients with RA. NRF2 directly influences the synthesis of antioxidant enzymes, which safeguard cells by inhibiting free radical production. SOD is essential for the scavenging of reactive oxygen species (ROS), which can ultimately reduce inflammation (Abd-El-Azim *et al.* 2024).

At the end of the experiment, levels of TNF-α, IL1, MMP 9, HO-1, NRF2, and SOD were evaluated, as Figure 3 demonstrates. Levels of TNF-α were increased by 2.8, 2.4, 1.9, and 1-fold in the positive control, the group treated with blank hyaluoleosomes, the AST suspension and the group treated AST-hyaluoleosomes, respectively in comparison with the negative control groups. TNF-α in the group treated with the AST-hyaluoleosomes was comparable to the negative control with no significant differences ($p < 0.0001$). On the other hand, levels of IL-1 were increased by 3.17, 1.86, 1.49, and 1.2-fold for the aforementioned groups in the same order. Previous research has shown that AST can inhibit bacterial lipopolysaccharide-induced production of TNF-α and IL-1β from peritoneal macrophages (Lu *et al.* 2004). Also, Jiang *et al.* reported that levels of the aforementioned mediators were decreased to those comparable to non-arthritic control animals after AST treatment (Jiang *et al.* 2010).

Levels of HO-1 were 100.3, 95.3, 89.2, 78.5, and 35.4 U/mL for the negative control, group treated with AST-hyaluoleosomes, AST suspension, blank hyaluoleosomes, and the positive control group, respectively. Furthermore, levels of NRF2 were reduced by 1.9, 1.3, 1.69, and 1.83 for the positive control, groups treated

with AST-hyaluoleosomes, AST suspension, blank hyaluoleosomes, respectively.

All treatment groups, including blank hyaluoleosomes demonstrated statistically significant differences from the positive control group, which may be ascribed to the inherent joint healing capabilities of hyaluoleosomes as a result of the incorporation of HA and the anti-inflammatory effects of oleic acid (Zewail *et al.* 2021a, Elhalmoushy *et al.* 2022, Santa-María *et al.* 2023). All treatment groups showed statistically significant differences among each other.

4.8.3. Histopathological study

The negative control group demonstrated normal histological structure of the articular surface in both H&E and Safranin O staining (Figures 4(A,B)). The positive control group showed severe destruction in the articular surface (arrows) in H&E (Figure 4(C)). Meanwhile, complete loss of proteoglycan in the articular surface was noted in the Safranin O staining (Figure 4(D)). In blank hyaluoleosomes, partial destruction of the articular surface (arrow) in H&E (Figure 4(I)) and fissure formation in the articular surface (arrow) with mild loss of proteoglycan (star) were also noted in Safranin O staining (Figure 4(J)). Moreover, the group treated with AST suspension demonstrated mild roughness of the articular surface (arrow) in the H&E stain (Figure 4(E)) and moderate loss of proteoglycan (star) in the articular surface in the Safranin O stain (Figure 4(F)). On the other hand, the normal histological structure of the articular surface in both stains was evident for AST hyaluoleosomes (Figures 4(G,H)).

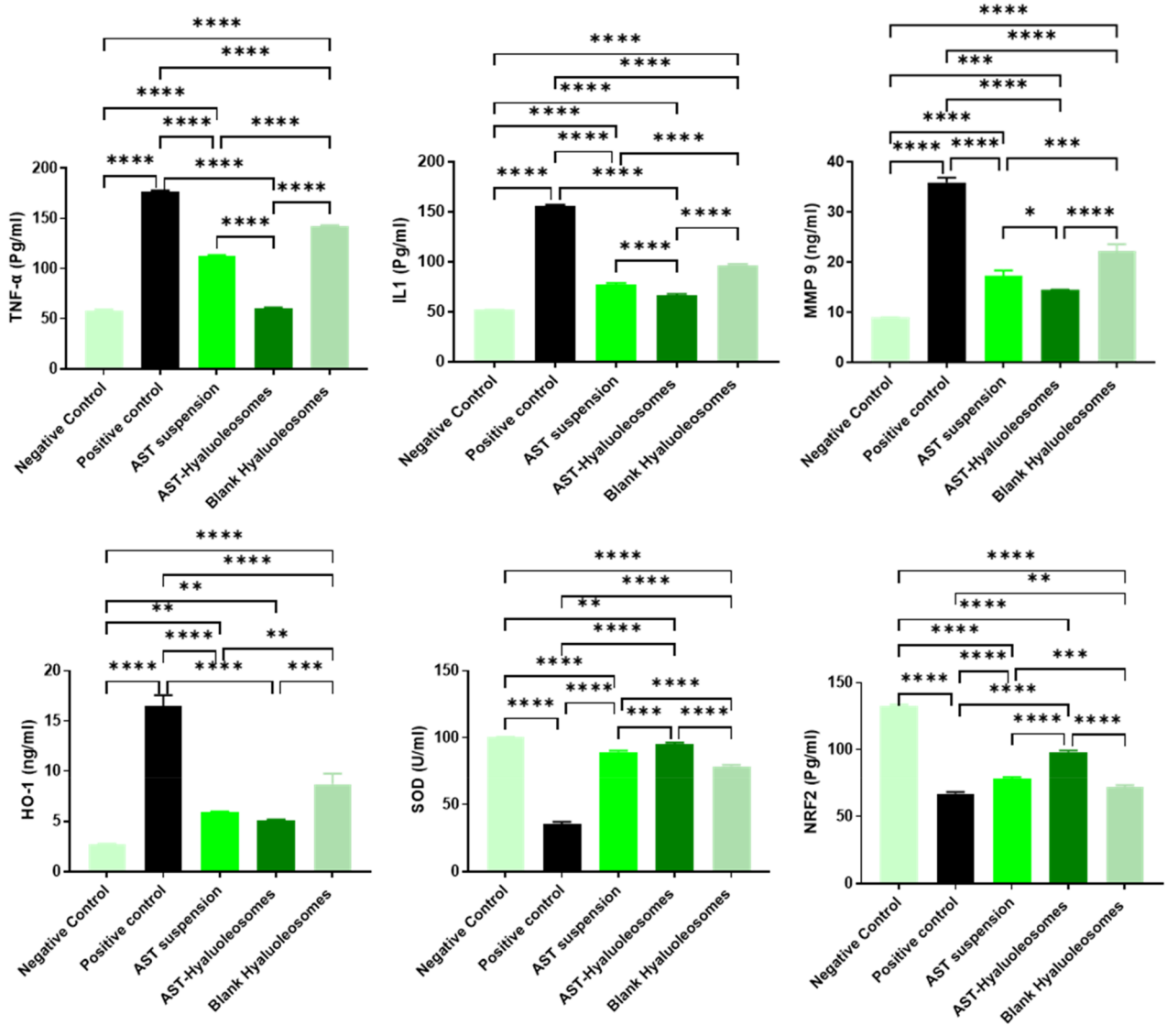


Figure 3. Levels of TNF-α, IL1, MMP9, HO-1, SOD, and NRF2 assessed using ELISA at the end of the experiment in different experimental groups where, $N = 4$, data were analysed using one-way ANOVA followed by Tukey test for multiple comparison, $^{**}p < 0.01$, $^{***}p < 0.001$, and $^{****}p < 0.0001$.

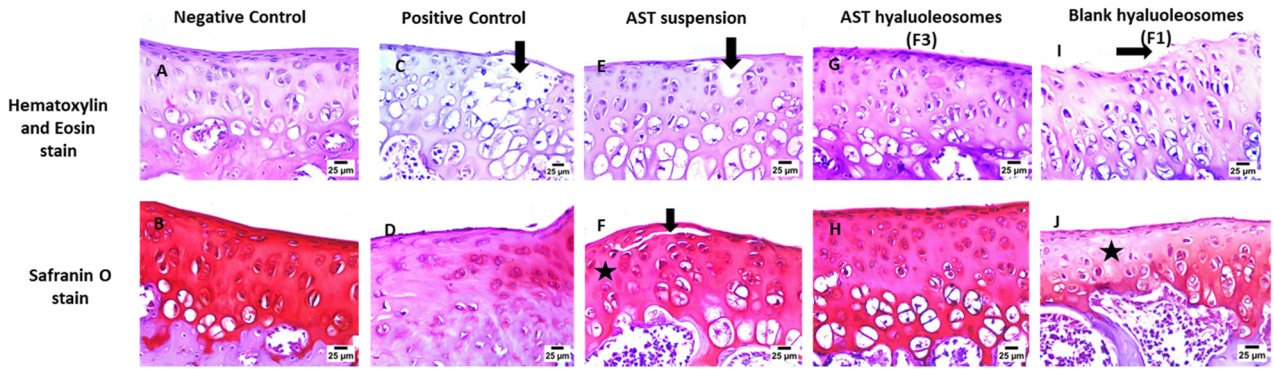


Figure 4. Histopathological examination of dissected joints after attaining with Haematoxylin and Eosin stain and Safranin O stain at the end of the experiment. Arrows demonstrate destruction of articular structure meanwhile stars represent the loss of proteoglycans.

Histopathological examination results are along with joint diameter and ELISA results. All the results confirmed the superior effect of AST-hyaluoleosomes over AST suspension and blank hyaluoleosomes. The significant improvement of joints in the group treated with blank hyaluoleosomes in comparison with the positive control may be attributed to the innate anti-inflammatory effects of hyaluoleosomes that is attributed to HA (Zewail *et al.* 2025c, 2025d) and oleic acid (Zewail *et al.* 2025b). This is in agreement with previous findings by Zewail *et al.*, who reported that blank hyalurosomes produced significant improvement in joint healing compared to the positive control in the AIA model (Zewail *et al.* 2025c). The joint healing effects of AST suspension may be ascribed to its high content of flavonoids. Natural flavonoids have the potential to inhibit NF-κB signalling, thereby reducing inflammatory responses, extracellular matrix degradation, and chondrocyte apoptosis (Ye and Zhou 2023). Among AST flavonoids is quercetin, which is known to mitigate RA inflammation as it can inhibit adenosine deaminase (ADA), which is an important inflammatory enzyme that increases joint stiffness and pain in RA. Also, it can reduce the levels of IL-1, IL6, TNF-α, rheumatoid factor, C-reactive protein, and anti-cyclic citrullinated peptide (El-Said *et al.* 2022). Moreover, Kaempferol 3-diglucoside is among AST flavonoids which exerts anti-inflammatory effects via altering the NLRP3/CASP1/GSDMD axis, hence inhibiting pyroptosis and suppressing hyperactive immune responses through T-cell proliferation (He *et al.* 2024). Furthermore, AST contains chlorogenic acid that can markedly suppress both nitric oxide generation and the expression of cyclooxygenase 2 (COX-2) and nitric oxide synthase (iNOS). Chlorogenic acid also can reduce pro-inflammatory cytokines (including IL-1β and TNF-α) and other inflammation-related indicators such as IL-6 in a dose-dependent manner. In addition, chlorogenic acid has the ability to decrease both the endotoxin-induced adherence of macrophages and the expression level of ninjurin1. Ultimately, chlorogenic acid obstructed the nuclear translocation of NF-κB (Hwang *et al.* 2014).

Nevertheless, AST contains unsaturated fatty acids like linoleic acid (Dipasquale *et al.* 2018), palmitic acid (Wu *et al.* 2014), and oleic acid (Zewail *et al.* 2025b), which are known of their anti-inflammatory potential.

Furthermore, caffeic acid and its derivatives exhibit significant antioxidant properties and possess notable anti-inflammatory effects both *in vitro* in RAW 264.7 macrophages an *in vivo* in carrageenan-induced inflammation as caffeic acid and its derivatives decreased paw oedema and reduced IL-1ß levels. These effects were ascribed to the scavenging of NO and the modulation of iNOS expression (Da Cunha *et al.* 2004).

Another factor that improved AST pharmacological effects is the MN-assisted administration, which aided in potentiating its pharmacological effects as they enhanced its penetration through the skin (Abd-El-Azim *et al.* 2023). Meanwhile, the superior effect of AST-hyaluoleosomes over AST suspension may be conferred to the impact of nanoencapsulation on enhancing the solubility of hydrophobic drugs like AST (Ho *et al.* 2009, Zewail 2021, Abd-El-Azim *et al.* 2022), besides the synergistic effect of HA and oleic acid incorporated in the structure of hyaluoleosomes (Zewail *et al.* 2025c).

5. Conclusion

This study investigates innovative applications of hyaluoleosomes and Ho-MNs for the use of AST in the treatment of RA. When compared to conventional methods of RA management, the benefits of MNs treatment far outweigh the costs. MNs improve drug absorption by delivering medication directly to the

affected areas; this may result in faster symptom alleviation and possibly less medication required. The approach of combing MNs and nanotechnology can reduce healthcare costs in the long run by reducing the risk of relapse and side effects. As a result of better patient adherence and fewer treatments are required, MN therapy can actually end up being more cost-effective than the conventional approaches.

Ethical approval

The Faculty of Pharmacy at Cairo University approved this experimental protocol with ethical approval number PT (3462).

Authors contributions

Haidy Abbas methodology, collected resources, analysed data, interpreted results, reviewed and edited the manuscript. Mariam Zewail and Heba Abd-El-Azim were responsible for the methodology, investigation, visualisation, and formal analysis reviewed and editing of the manuscript. Nesrine El Sayed was in charge of the experimental design visualisation and formal analysis as well as the *in vivo* animal study. Mohamed Fayez Dekinash and Reham Mustafa methodology, investigation, visualisation, and formal analysis reviewed the manuscript. All authors have read and agreed to the published version of the manuscript.

Disclosure statement

No potential conflict of interest was reported by the author(s).

Funding

No funding resources were provided to conduct the current study.

Data availability statement

All data are provided in the manuscript. The research data associated with the paper is all available.

References

Abbas, H., El-Deeb, N.M., and Zewail, M., 2021. PLA-coated Imwitor® 900 K-based herbal colloidal carriers as novel candidates for the intra-articular treatment of arthritis. *Pharmaceutical development and technology*, 26 (6), 682–692. doi: 10.1080/10837450.2021.1920617.

Abbas, H., *et al.*, 2022. Development and evaluation of novel leflunomide SPION bioemulsomes for the intra-articular treatment of arthritis. *Pharmaceutics*, 14 (10), 2005. doi: 10.3390/pharmaceutics14102005.

Abdelalim, L.R., Elnaggar, Y.S., and Abdallah, O.Y., 2020. Oleosomes encapsulating sildenafil citrate as potential topical nanotherapy for palmar plantar erythrodysesthesia with high *ex vivo* permeation and deposition. *AAPS PharmSciTech*, 21 (8), 310. doi: 10.1208/s12249-020-01862-2.

Abd-El-Azim, H., *et al.*, 2022. Hollow microneedle assisted intradermal delivery of hypericin lipid nanocapsules with light enabled photodynamic therapy against skin cancer. *Journal of controlled release*, 348, 849–869. doi: 10.1016/j.jconrel.2022.06.027.

Abd-El-Azim, H., *et al.*, 2023. Non-invasive management of rheumatoid arthritis using hollow microneedles as a tool for transdermal delivery of teriflunomide loaded solid lipid nanoparticles. *International journal of pharmaceutics*, 644, 123334. doi: 10.1016/j.ijpharm.2023.123334.

Abd-El-Azim, H., *et al.*, 2024. Hypericin emulsomes combined with hollow microneedles as a non-invasive photodynamic platform for rheumatoid arthritis treatment. *International journal of pharmaceutics*, 653, 123876. doi: 10.1016/j.ijpharm.2024.123876.

Ahmed, S., Kassem, M.A., and Sayed, S., 2020. Bilosomes as promising nanovesicular carriers for improved transdermal delivery: construction, *in vitro* optimization, *ex vivo* permeation and *in vivo* evaluation. *International journal of nanomedicine*, 15, 9783–9798. doi: 10.2147/IJN.S278688.

Anita, C., *et al.*, 2021. Topical nanocarriers for management of rheumatoid arthritis: a review. *Biomedicine & pharmacotherapy*, 141, 111880. doi: 10.1016/j.biopha.2021.111880.

Arora, G., Malik, K., and Singh, I., 2011. Formulation and evaluation of mucoadhesive matrix tablets of taro gum: optimization using response surface methodology. *Polimery w medycynie*, 41 (2), 23–34.

Bancroft, J.D. and Gamble, M., 2008. *Theory and practice of histological techniques*. Churchill Livingstone Elsevier, Philadelphia.

Boskabady, M.H., *et al.*, 2011. Pharmacological effects of *Rosa damascena*. *Iranian journal of basic medical sciences*, 14 (4), 295–307.

Bratkov, V.M., *et al.*, 2016. Flavonoids from the genus *Astragalus*: phytochemistry and biological activity. *Pharmacognosy reviews*, 10 (19), 11–32. doi: 10.4103/0973-7847.176550.

Buiarelli, F., *et al.*, 2010. Identification of hydroxycinnamic acid–tartaric acid esters in wine by HPLC–tandem mass spectrometry. *Food chemistry*, 123 (3), 827–833. doi: 10.1016/j.foodchem.2010.05.017.

Chaturvedula, V.S.P. and Prakash, I., 2013. Flavonoids from Astragalus propinquus. *Journal of Chemical and Pharmaceutical Research*, 5 (1), 261–265.

Cheng, T., *et al.*, 2019. Hybrid multidimensional data acquisition and data processing strategy for comprehensive characterization of known, unknown and isomeric compounds from the compound Dan Zhi Tablet by UPLC-TWIMS-QTOFMS. *RSC advances*, 9 (16), 8714–8727. doi: 10.1039/c8ra10100k.

Choudhary, N., Bhatt, L.K., and Prabhavalkar, K.S., 2018. Experimental animal models for rheumatoid arthritis. *Immunopharmacology and immunotoxicology*, 40 (3), 193–200. doi: 10.1080/08923973.2018.1434793.

Da Cunha, F.M., *et al.*, 2004. Caffeic acid derivatives: *in vitro* and *in vivo* anti-inflammatory properties. *Free radical research*, 38 (11), 1241–1253. doi: 10.1080/10715760400016139.

Dekinash, M.F., *et al.*, 2022. Insights into HPLC-MS/MS analysis, antioxidant and cytotoxic activity of *Astragalus fruticosus* against different types of cancer cell lines. *Pharmaceuticals*, 15 (11), 1406. doi: 10.3390/ph15111406.

Della Corte, A., *et al.*, 2015. A rapid LC–MS/MS method for quantitative profiling of fatty acids, sterols, glycerolipids, glycerophospholipids and sphingolipids in grapes. *Talanta*, 140, 52–61. doi: 10.1016/j.talanta.2015.03.003.

Dipasquale, D., *et al.*, 2018. Anti-inflammatory effects of conjugated linoleic acid isomers and essential fatty acids in bovine mammary epithelial cells. *Animal*, 12 (10), 2108–2114. doi: 10.1017/S1751731117003676.

Dragicevic-Curic, N., *et al.*, 2010. Surface charged temoporfin-loaded flexible vesicles: *in vitro* skin penetration studies and stability. *International journal of pharmaceutics*, 384 (1–2), 100–108. doi: 10.1016/j.ijpharm.2009.10.006.

Du, Y., *et al.*, 2022. A critical review of *Astragalus* polysaccharides: from therapeutic mechanisms to pharmaceutics. *Biomedicine & pharmacotherapy*, 147, 112654. doi: 10.1016/j.biopha.2022.112654.

Elhalmoushy, P.M., *et al.*, 2022. Novel berberine-loaded hyalurosomes as a promising nanodermatological treatment for vitiligo: biochemical, biological and gene expression studies. *International journal of pharmaceutics*, 615, 121523. doi: 10.1016/j.ijpharm.2022.121523.

Elhalmoushy, P.M., *et al.*, 2023. Elaboration of novel gel-core oleosomes encapsulating phytoconstituent for targeted topical delivery in a vitiligo-induced mouse model: focus on antioxidant and anti-inflammatory pathways. *Journal of drug delivery science and technology*, 80, 104119. doi: 10.1016/j.jddst.2022.104119.

Elmowafy, M., 2021. Skin penetration/permeation success determinants of nanocarriers: pursuit of a perfect formulation. *Colloids and surfaces. B, biointerfaces*, 203, 111748. doi: 10.1016/j.colsurfb.2021.111748.

El-Said, K.S., *et al.*, 2022. Quercetin mitigates rheumatoid arthritis by inhibiting adenosine deaminase in rats. *Molecular medicine*, 28 (1), 24. doi: 10.1186/s10020-022-00432-5.

Elsheikh, M.A., *et al.*, 2023. Dual-effects of caffeinated hyalurosomes as a nano-cosmeceutical gel counteracting UV-induced skin ageing. *International journal of pharmaceutics: X*, 5, 100170. doi: 10.1016/j.ijpx.2023.100170.

Farag, M.A., *et al.*, 2014. Metabolomic fingerprints of 21 date palm fruit varieties from Egypt using UPLC/PDA/ESI–qTOF-MS and GC–MS analyzed by chemometrics. *Food research international*, 64, 218–226. doi: 10.1016/j.foodres.2014.06.021.

Frański, R., *et al.*, 2019. Signals of diagnostic ions in the product ion spectra of $[M-H]^-$ ions of methoxylated flavonoids. *Rapid communications in mass spectrometry*, 33 (1), 125–132. doi: 10.1002/rcm.8316.

Fu, J., *et al.*, 2014. Review of the botanical characteristics, phytochemistry, and pharmacology of *Astragalus membranaceus* (Huangqi). *Phytotherapy research*, 28 (9), 1275–1283. doi: 10.1002/ptr.5188.

Gowda, B.J., *et al.*, 2023. Microneedles as a momentous platform for psoriasis therapy and diagnosis: a state-of-the-art review. *International journal of pharmaceutics*, 632, 122591. doi: 10.1016/j.ijpharm.2023.122591.

He, X., *et al.*, 2024. Study of kaempferol in the treatment of rheumatoid arthritis through modulation of the NLRP3/CASP1/GSDMD axis and T-cell activation: based on network pharmacology, single-cell analysis, and experimental validation. *International immunopharmacology*, 143 (Pt 1), 113357. doi: 10.1016/j.intimp.2024.113357.

Ho, Y.-F., *et al.*, 2009. Lipid-mediated preferential localization of hypericin in lipid membranes. *Biochimica et biophysica acta*, 1788 (6), 1287–1295. doi: 10.1016/j.bbamem.2009.01.017.

Hu, J., *et al.*, 2022. Seleno-amino acids in vegetables: a review of their forms and metabolism. *Frontiers in plant science*, 13, 804368. doi: 10.3389/fpls.2022.804368.

Hwang, S.J., *et al.*, 2014. Anti-inflammatory effects of chlorogenic acid in lipopolysaccharide-stimulated RAW 264.7 cells. *Inflammation research*, 63 (1), 81–90. doi: 10.1007/s00011-013-0674-4.

Ionkova, I., *et al.*, 2014. Recent progress in phytochemistry, pharmacology and biotechnology of *Astragalus saponins*. *Phytochemistry reviews*, 13 (2), 343–374. doi: 10.1007/s11101-014-9347-3.

Jiang, J.B., *et al.*, 2010. Therapeutic effects of astragalus polysaccharides on inflammation and synovial apoptosis in rats with adjuvant-induced arthritis. *International journal of rheumatic diseases*, 13 (4), 396–405. doi: 10.1111/j.1756-185X.2010.01555.x.

Jiang, R.-W., *et al.*, 2005. Chemistry and biological activities of caffeic acid derivatives from *Salvia miltiorrhiza*. *Current medicinal chemistry*, 12 (2), 237–246. doi: 10.2174/0929867053363397.

Jiang, S.J. and Zhou, X.J., 2003. Examination of the mechanism of oleic acid-induced percutaneous penetration enhancement: an ultrastructural study. *Biological & pharmaceutical bulletin*, 26 (1), 66–68. doi: 10.1248/bpb.26.66.

Kamel, R., Salama, A.H., and Mahmoud, A.A., 2016. Development and optimization of self-assembling nanosystem for intra-articular delivery of indomethacin. *International journal of pharmaceutics*, 515 (1–2), 657–668. doi: 10.1016/j.ijpharm.2016.10.063.

Kay, J. and Calabrese, L., 2004. The role of interleukin-1 in the pathogenesis of rheumatoid arthritis. *Rheumatology*, 43 Suppl 3 (suppl_3), iii2–iii9. doi: 10.1093/rheumatology/keh201.

Kerwin, J.L., Wiens, A.M., and Ericsson, L.H., 1996. Identification of fatty acids by electrospray mass spectrometry and tandem mass spectrometry. *Journal of mass spectrometry*, 31 (2), 184–192. doi: 10.1002/(SICI)1096-9888(199602)31:2<184::AID-JMS283>3.0.CO;2-2.

Koch, E., *et al.*, 2021. Rapid quantification of fatty acids in plant oils and biological samples by LC-MS. *Analytical and bioanalytical chemistry*, 413 (21), 5439–5451. doi: 10.1007/s00216-021-03525-y.

Kurek, E., *et al.*, 2020. Searching for low molecular weight seleno-compounds in sprouts by mass spectrometry. *Molecules*, 25 (12), 2870. doi: 10.3390/molecules25122870.

Liu, X.-Y., *et al.*, 2017. Protective effects of total flavonoids of *Astragalus* against adjuvant-induced arthritis in rats by regulating OPG/RANKL/NF-κB pathway. *International immunopharmacology*, 44, 105–114. doi: 10.1016/j.intimp.2017.01.010.

Lu, G., *et al.*, 2019. Nanoparticles containing hyaluronan acid and astragalus polysaccharides for treating osteoarthritis. *International journal of polymer science*, 2019 (1), 1–6. doi: 10.1155/2019/8143528.

Lu, J., Yang, Y., and Chen, M., 2004. Effect of astragalus polysaccharides on IL-1, NO and TNF-α secreted by lipopolysaccharide-induced normal rat peritoneal macrophages. *Acta universitatis medicinalis Anhui*, 39 (2), 139–141.

Makled, S., *et al.*, 2024. Melatonin hyalurosomes in collagen thermosensitive gel as a potential repurposing approach for rheumatoid arthritis management via the intra-articular route. *International journal of pharmaceutics*, 661, 124449. doi: 10.1016/j.ijpharm.2024.124449.

Manca, M.L., *et al.*, 2019. Potential therapeutic effect of curcumin loaded hyalurosomes against inflammatory and oxidative processes involved in the pathogenesis of rheumatoid arthritis: the use of fibroblast-like synovial cells cultured in synovial fluid. *European journal of pharmaceutics and biopharmaceutics*, 136, 84–92. doi: 10.1016/j.ejpb.2019.01.012.

Maresca, M., *et al.*, 2017. Pain relieving and protective effects of astragalus hydroalcoholic extract in rat arthritis models. *The journal of pharmacy and pharmacology*, 69 (12), 1858–1870. doi: 10.1111/jphp.12828.

Morilla, M.J. and Romero, E.L., 2015. Ultradeformable phospholipid vesicles as a drug delivery system: a review. *Research and reports in transdermal drug delivery*, 4, 55–69.

Moussa, A.Y., *et al.*, 2023. Green preparation and evaluation of the anti-psoriatic activity of vesicular elastic nanocarriers of kojic acid from *Aspergillus oryzae* N12: repurposing of a dermo-cosmetic lead. *Archiv der pharmazie*, 357 (11), e2400410.

Murad, A.M., *et al.*, 2014. Mass spectrometry characterisation of fatty acids from metabolically engineered soybean seeds. *Analytical and bioanalytical chemistry*, 406 (12), 2873–2883. doi: 10.1007/s00216-014-7709-8.

Negi, S., *et al.*, 2024. Co-delivery of aceclofenac and methotrexate nanoparticles presents an effective treatment for rheumatoid arthritis. *International journal of nanomedicine*, 19, 2149–2177. doi: 10.2147/IJN.S439359.

Rahman, H.S., *et al.*, 2013. Zerumbone-loaded nanostructured lipid carriers: preparation, characterization, and antileukemic effect. *International journal of nanomedicine*, 8, 2769–2781. doi: 10.2147/IJN.S45313.

Ralphs, M., *et al.*, 2008. Relationship between the endophyte *Embellisia* spp. and the toxic alkaloid swainsonine in major locoweed species (*Astragalus* and *Oxytropis*). *Journal of chemical ecology*, 34 (1), 32–38. doi: 10.1007/s10886-007-9399-6.

Recio, M.C., Andujar, I., and Rios, J.L., 2012. Anti-inflammatory agents from plants: progress and potential. *Current medicinal chemistry*, 19 (14), 2088–2103.

Santa-María, C., *et al.*, 2023. Update on anti-inflammatory molecular mechanisms induced by oleic acid. *Nutrients*, 15 (1), 224. doi: 10.3390/nu15010224.

Selim, D.A., *et al.*, 2023. Comparative metabolomics of the different fractions of two saltwort (*Salsola* L.) species in relation to their anti-inflammatory activity. *Food bioscience*, 51, 102306. doi: 10.1016/j.fbio.2022.102306.

Shawky, E., *et al.*, 2022. Comparative metabolomics analysis of bioactive constituents of the leaves of different *Trigonella* species: correlation study to α-amylase and α-glycosidase inhibitory effects. *Industrial crops and products*, 182, 114947. doi: 10.1016/j.indcrop.2022.114947.

Sheng, Z., *et al.*, 2021. UHPLC–MS/MS analysis on flavonoids composition in *Astragalus membranaceus* and their antioxidant activity. *Antioxidants*, 10 (11), 1852. doi: 10.3390/antiox10111852.

Silva, T., Oliveira, C., and Borges, F., 2014. Caffeic acid derivatives, analogs and applications: a patent review (2009–2013). *Expert opinion on therapeutic patents*, 24 (11), 1257–1270. doi: 10.1517/13543776.2014.959492.

Simons, R., *et al.*, 2009. A rapid screening method for prenylated flavonoids with ultra-high-performance liquid chromatography/electrospray ionisation mass spectrometry in licorice root extracts. *Rapid communications in mass spectrometry*, 23 (19), 3083–3093. doi: 10.1002/rcm.4215.

Smolen, J.S. and Aletaha, D., 2015. Rheumatoid arthritis therapy reappraisal: strategies, opportunities and challenges. *Nature reviews. Rheumatology*, 11 (5), 276–289. doi: 10.1038/nrrheum.2015.8.

Soni, G. and Yadav, K.S., 2014. High encapsulation efficiency of poloxamer-based injectable thermoresponsive hydrogels of etoposide. *Pharmaceutical development and technology*, 19 (6), 651–661. doi: 10.3109/10837450.2013.819014.

Verotta, L., *et al.*, 1998. Cycloartane triterpene glycosides from *Astragalus sieberi*. *Phytochemistry*, 48 (8), 1403–1409. doi: 10.1016/S0031-9422(98)00042-9.

Wang, J., *et al.*, 2022. Promising strategies for transdermal delivery of arthritis drugs: microneedle systems. *Pharmaceutics*, 14 (8), 1736. doi: 10.3390/pharmaceutics14081736.

Wang, Q., *et al.*, 2021. Nanomedicines for the treatment of rheumatoid arthritis: State of art and potential therapeutic strategies. *Acta pharmaceutica sinica. B*, 11 (5), 1158–1174. doi: 10.1016/j.apsb.2021.03.013.

Wang, S., *et al.*, 2020. Recent advances in nanotheranostics for treat-to-target of rheumatoid arthritis. *Advanced healthcare materials*, 9 (6), e1901541. doi: 10.1002/adhm.201901541.

Wei, J.C., *et al.*, 2017. Allometric scaling of skin thickness, elasticity, viscoelasticity to mass for micro-medical device translation: from mice, rats, rabbits, pigs to humans. *Scientific reports*, 7 (1), 15885. doi: 10.1038/s41598-017-15830-7.

Willems, J.L., *et al.*, 2016. Analysis of a series of chlorogenic acid isomers using differential ion mobility and tandem mass spectrometry. *Analytica chimica acta*, 933, 164–174. doi: 10.1016/j.aca.2016.05.041.

Witika, B.A., *et al.*, 2020. Biocompatibility of biomaterials for nanoencapsulation: Current approaches. *Nanomaterials*, 10 (9), 1649. doi: 10.3390/nano10091649.

Wu, D., *et al.*, 2014. Palmitic acid exerts pro-inflammatory effects on vascular smooth muscle cells by inducing the expression of C-reactive protein, inducible nitric oxide synthase and tumor necrosis factor-α. *International journal of molecular medicine*, 34 (6), 1706–1712. doi: 10.3892/ijmm.2014.1942.

Yang, B., *et al.*, 2023. A multi-component nano-co-delivery system utilizing astragalus polysaccharides as carriers for improving biopharmaceutical properties of astragalus flavonoids. *International journal of nanomedicine*, 18, 6705–6724. doi: 10.2147/IJN.S434196.

Ye, Y. and Zhou, J., 2023. The protective activity of natural flavonoids against osteoarthritis by targeting NF-κB signaling pathway. *Frontiers in endocrinology*, 14, 1117489. doi: 10.3389/fendo.2023.1117489.

Zewail, M., 2021. Folic acid decorated chitosan-coated solid lipid nanoparticles for the oral treatment of rheumatoid arthritis. *Therapeutic delivery*, 12 (4), 297–310. doi: 10.4155/tde-2020-0123.

Zewail, M., 2024. Leflunomide nanocarriers: a new prospect of therapeutic applications. *Journal of microencapsulation*, 41 (8), 715–738. doi: 10.1080/02652048.2024.2407373.

Zewail, M., *et al.*, 2019. Coated nanostructured lipid carriers targeting the joints–an effective and safe approach for the oral management of rheumatoid arthritis. *International journal of pharmaceutics*, 567, 118447. doi: 10.1016/j.ijpharm.2019.118447.

Zewail, M., *et al.*, 2021a. Synergistic and receptor-mediated targeting of arthritic joints via intra-articular injectable smart hydrogels containing leflunomide-loaded lipid nanocarriers. *Drug delivery and translational research*, 11 (6), 2496–2519. doi: 10.1007/s13346-021-00992-9.

Zewail, M., *et al.*, 2022a. Hyaluronic acid coated teriflunomide (A771726) loaded lipid carriers for the oral management of rheumatoid arthritis. *International journal of pharmaceutics*, 623, 121939. doi: 10.1016/j.ijpharm.2022.121939.

Zewail, M., *et al.*, 2022b. Lipidic cubic-phase leflunomide nanoparticles (cubosomes) as a potential tool for breast cancer management. *Drug delivery*, 29 (1), 1663–1674. doi: 10.1080/10717544.2022.2079770.

Zewail, M., *et al.*, 2024. Combined photodynamic therapy and hollow microneedle approach for effective non-invasive delivery of hypericin for the management of imiquimod-induced psoriasis. *Journal of drug targeting*, 32 (8), 941–952. doi: 10.1080/1061186X.2024.2365930.

Zewail, M., *et al.*, 2025a. Intradermal delivery of teriflunomide loaded emulsomes using hollow microneedles for effective minimally invasive psoriasis management. *European journal of pharmaceutics and biopharmaceutics*, 210, 114692. doi: 10.1016/j.ejpb.2025.114692.

Zewail, M., *et al.*, 2025b. Intradermal delivery of nanohybrid thermosensitive hydrogels loaded with chondroitin sulphate coated pomegranate lipid carriers via hollow microneedles for effective rheumatoid arthritis management. *Journal of drug delivery science and technology*, 112, 107234. doi: 10.1016/j.jddst.2025.107234.

Zewail, M., *et al.*, 2025c. Innovative rheumatoid arthritis management using injection replacement approach via dual therapeutic effects of hyalurosomes-encapsulated luteolin and dexamethasone. *Colloids and surfaces. B, biointerfaces*, 249, 114497. doi: 10.1016/j.colsurfb.2025.114497.

Zewail, M., *et al.*, 2025d. Unveiling the synergistic impact of cocktail nanohyalurosomes encapsulating berberine and dexamethasone in managing rheumatoid arthritis: *in-vitro* evaluation and biological studies. *Journal of microencapsulation*, 42 (5), 503–518. doi: 10.1080/02652048.2025.2498963.

Zewail, M., Nafee, N., and Boraie, N., 2021b. Intra-articular dual drug delivery for synergistic rheumatoid arthritis treatment. *Journal of pharmaceutical sciences*, 110 (7), 2808–2822. doi: 10.1016/j.xphs.2021.04.001.

Zhang, Y., *et al.*, 2016. Oleanane type saponins from the stems of *Astragalus membranaceus* (Fisch.) Bge. var. *mongholicus* (Bge.) Hsiao. *Fitoterapia*, 109, 99–105. doi: 10.1016/j.fitote.2015.12.006.

Zou, X., *et al.*, 2022. Molecular recognition and quantitative analysis of free and combinative selenium speciation in selenium-enriched millets using HPLC-ESI-MS/MS. *Journal of food composition and analysis*, 106, 104333. doi: 10.1016/j.jfca.2021.104333.